

Anomaly detection in chest radiographs with a weakly supervised flow-based deep learning method

Hisaichi Shibata^{a,*}, Shouhei Hanaoka^b, Yukihiro Nomura^a,
Takahiro Nakao^c, Issei Sato^{b,d,e}, Naoto Hayashi^a, Osamu Abe^{b,c}

^a*Department of Computational Diagnostic Radiology and Preventive Medicine, The University of Tokyo Hospital, 7-3-1 Hongo, Bunkyo-ku, Tokyo, 113-8655 Japan*

^b*Department of Radiology, The University of Tokyo Hospital, 7-3-1 Hongo, Bunkyo-ku, Tokyo, 113-8655 Japan*

^c*Division of Radiology and Biomedical Engineering, Graduate School of Medicine, The University of Tokyo, 7-3-1 Hongo, Bunkyo-ku, Tokyo, 113-8656 Japan*

^d*Department of Complexity Science and Engineering, Graduate School of Frontier Sciences, The University of Tokyo, 5-1-5 Kashiwanoha, Kashiwa, Chiba, 277-8561 Japan*

^e*Center for Advanced Intelligence Project, RIKEN, 1-4-1 Nihonbashi, Chuo-ku, Tokyo, 103-0027 Japan*

Abstract

Preventing the oversight of anomalies in chest X-ray radiographs (CXRs) during diagnosis is a crucial issue. Deep learning (DL)-based anomaly detection methods are rapidly growing in popularity, and provide effective solutions to the problem, but the workload in labeling CXRs during the training procedure remains heavy. To reduce the workload, a novel anomaly detection method for CXRs based on weakly supervised DL is presented in this study. The DL is based on a flow-based deep neural network (DNN) framework with which two normality metrics (logarithm likelihood and logarithm likelihood ratio) can be calculated. With this method, only one set of normal CXRs requires labeling to train the DNN, then the normality of any unknown CXR can be evaluated. The area under the receiver operation characteristic curve acquired with the logarithm likelihood ratio metric (≈ 0.783) was greater than that obtained with the logarithm likelihood metric, and was a value comparable to those in previous studies where other weakly supervised DNNs were implemented.

*Corresponding Author

Email address: sh-tky@umin.ac.jp (Hisaichi Shibata)

Accuracy, Workload	<u>Training input(s)</u>	<u>Category</u>
	labels for all CXRs AUC: 0.99 [4,5]	Supervised
	labels only for partial CXRs AUC: 0.84 [7]	Semi-Supervised
	labels only for normal CXRs AUC: 0.80 [6] AUC: ~0.87 (Present)	Weakly Supervised

Figure 1: Classification of DL methods with reference to CXR image analysis.

Keywords: Anomaly Detection, Chest X-ray Radiographs, Weakly Supervised, Deep Learning

1. Introduction

Chest X-ray radiographs (CXRs) are widely adopted to diagnose various diseases including pneumonia, lung cancer, pneumothorax, pleural effusion, lung metastasis, bone metastases, heart disease, and mediastinal tumors. Physicians must detect and then classify such diseases from a large number of CXRs in a realistic period [1], and this is the first step in providing appropriate medical treatment such as diagnosis using computer tomography. Therefore, in many cases, anomaly detection in CXRs is one of the most important steps in medical treatment; hence, oversights of lesions must be prevented. To prevent such oversights and hopefully reduce the workload in the detection procedure, a computer-assisted anomaly detection system is strongly desired.

Deep learning (DL)-based image recognition technologies can potentially reduce oversights and the workload of interpreters because of the rapid increase in the precision of image recognition [2, 3]. Many previous studies on anomaly detection in CXRs with DL-based technologies have been reported [4, 5, 6, 7]. Previous studies, in which DL-based technology was applied to detect anomalies or kinds of lesion in CXRs can be classified into various categories as shown in Fig. 1. Supervised DL methods [4, 5] can attain the highest area under the curve (AUC) among the categories, but a heavy

workload is required to prepare labels for unknown CXRs. Semi- or weakly supervised DL methods [6, 7] have much lower workloads, but also a lower AUC. The present study is devoted to the development of a weakly supervised DL methods so that the workload required for labeling is minimized.

Several studies have been carried out on the use of the semi- or weakly supervised learning DL methods in medical image analysis. One of the most recent weakly supervised learning utilized for CXRs appeared in [8], in which lesion domains in CXRs were automatically localized and visualized. However, in this weakly supervised DL method, it was necessary to label different types of lesion to train deep neural networks (DNNs), which is a crucial difference from the present study. With reference to labeling, the only requirement of our method is that all the CXRs in a certain training set are normal. In [9], to detect images different from lateral CXRs, i.e., out-of-distribution (OOD) samples, a metric based on the Mahalanobis distance was applied. However, our interest in the present study is anomaly detection within CXRs of the same type, and it is considered to be more challenging to detect an anomaly when the metric is applied. Tang et al. [6] followed a similar approach to the present study. In their work, a network inherited from generative adversarial networks (GANs) [10] and an evaluation metric containing hyperparameters to be tuned were utilized, which are crucial differences from the present work.

A weakly supervised DL method in which there is no necessity to train DNNs by labeling the kind of lesion or even tune hyperparameters in the metric is attractive for the following reasons. Firstly, the workload of interpreters in labeling CXRs can be reduced. Secondly, higher robustness can potentially be achieved because the method can handle unknown lesions not included in the training set of the DNN. Thirdly, the computational cost of the hyperparameter tuning procedure can be eliminated.

In the present study, such a weakly supervised DL method of detecting anomalies in frontal-view CXRs is introduced, implemented, and tested, and its efficacy is validated. The rest of this paper is constituted as follows. In Sec. 2, two methods with different metrics for anomaly detection in CXRs are introduced. In Sec. 3, the preparation of setup and dataset used to execute numerical experiments is reported. In Sec. 4, the results of experiments are given. In Sec. 5, a discussion based on the results of the experiments is presented. In Sec. 6, the present study is summarized.

2. Methods

As DL methods to detect anomalies in CXRs or classify CXRs, two models are mainly used from the viewpoint of the evaluation metric to be optimized: the discriminative model and the generative model.

The discriminative model can output $p(\mathbf{y}_i|\mathbf{x}_j)$, where p is the probability that the i th input vector \mathbf{x}_i belongs to the j th category \mathbf{y}_j . Therefore, the model can directly classify input CXRs by choosing the category with which the probability takes the largest value. However, training with samples in all the categories is necessary.

The generative model can directly output the likelihood that \mathbf{x}_i is well approximated with the distribution of category \mathbf{y}_j , i.e., $p(\mathbf{x}_i|\mathbf{y}_j)$, while only knowing the distribution of a certain dataset (herein \mathbf{y}_j), i.e., the information that all the CXRs in a certain training set are normal in this study.

If the characteristic of the generative model is inherited, the model is able to directly derive the likelihood that a certain CXR belongs to a normal CXR set, i.e., $p(\mathbf{x}_i|\text{normal})$, without the training using the labeled dataset in all categories. Moreover, with this model, it is possible to estimate a quantity that is proportional to $p(\mathbf{y}_i|\mathbf{x}_j)$ in addition to $p(\mathbf{x}_i|\mathbf{y}_j)$ by utilizing the technique described later in this section.

To obtain these prospective benefits, in the present study the generative model and two metrics based on the likelihood are adopted. To facilitate our explanation, a CXR set, $\mathcal{S}_{\text{normal}}^{\text{train}}$, which only contains normal CXRs for training, and two other CXR sets, $\mathcal{S}_{\text{all}}^{\text{train}}$ and $\mathcal{S}_{\text{all}}^{\text{test}}$, which contain both normal and abnormal CXRs, for training and testing, respectively are defined.

Flowcharts of the methods to be introduced hereafter are shown in Figs. 2(a) and (b), together with those of the discriminative model and GANs, to be discussed in detail in Sec. 5.

The first metric introduced herein directly uses a logarithm likelihood, $\log p(\mathbf{x}_i|\text{normal})$, which represents how accurately an input CXR (\mathbf{x}_i) is likely to be approximated with a DNN trained with normal CXRs only. The larger the value of $\log p(\mathbf{x}_i|\text{normal})$, the higher the probability that \mathbf{x}_i belongs to the space spanned with the training data, i.e., that \mathbf{x}_i is a normal CXR.

To explicitly compute the metric, a logarithm likelihood estimator is required. In this study, as the estimator, Glow [11], which is one of the flow-based generative DL frameworks, is adopted.

The concept of flow-based DNNs is shown in Fig. 3. In flow-based DNNs, space variables corresponding to input CXRs ($\mathbf{x}_i^{\text{train/test}} \in \mathbb{R}^N$), where N

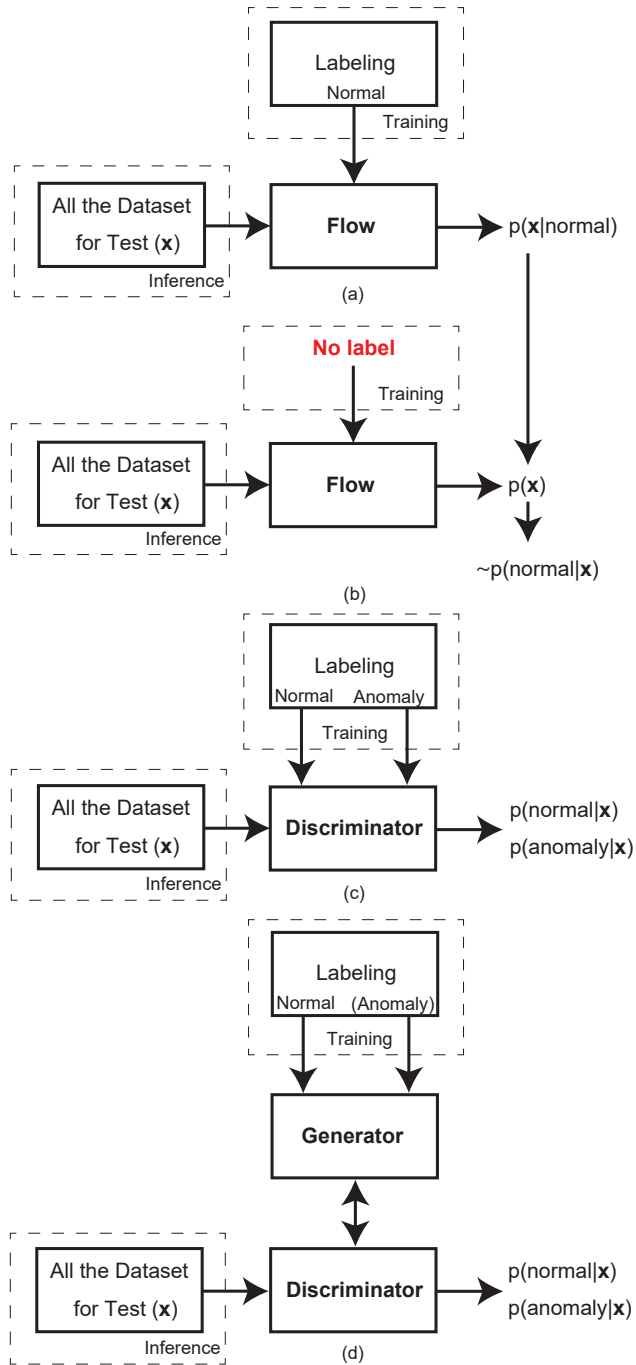


Figure 2: Flowchart of anomaly detection; generators appearing in flow-based models are labeled as “Flow”: (a) with the proposed model using the first metric, (b) with the proposed model using the second metric, (c) with the discriminative model used as a binary classifier, (d) with the GAN model used as a binary classifier.

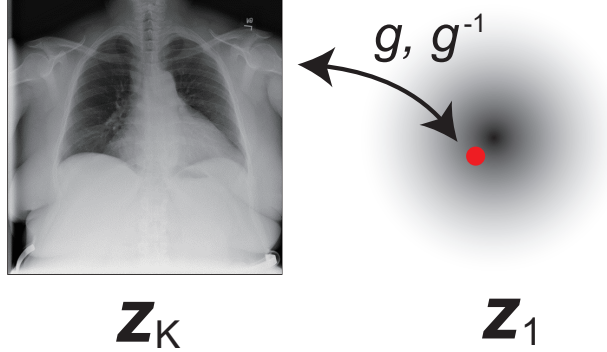


Figure 3: Overview of flow-based DNN, where $g = f_1 \circ f_2 \circ \dots \circ f_{K-1}$, and the red point indicates the destination of the transformation onto the high-dimensional Gaussian distribution.

is the dimension of input images, are recursively projected onto a latent space variable ($\mathbf{z}_i \in \mathbb{R}^N$) using invertible transformations $\mathbf{z}_{i,k+1} = \mathbf{f}_k(\mathbf{z}_{i,k})$ for $k = 1, \dots, (K-1)$, where K is a constant, $\mathbf{z}_{i,K} = \mathbf{x}_i$, and $\mathbf{z}_{i,1} \in \mathbb{R}^N$ is targeted as a point typically in a multivariate high-dimensional Gaussian distribution. The transformation of logarithm probability density functions between that of the targeted distribution and the input vector, e.g., CXRs, is given by

$$\log p(\mathbf{z}_{i,K}) = \log p(\mathbf{z}_{i,1}) + \sum_{k=1}^K \log \det \left| \left(\frac{d\mathbf{f}_k}{d\mathbf{f}_{k-1}} \right) \right| \quad (1)$$

where $\mathbf{f}_0 \triangleq \mathbf{x}_i$ and $\mathbf{f}_K \triangleq \mathbf{z}_{i,1}$. For details of the flow-based generative model, see [11].

The procedures to compute the first metric is summarized as follows:

1. Prepare input data
 - (a) Gather CXR set, $\mathcal{S}_{\text{normal}}^{\text{train}}$
 - (b) Gather CXR set, $\mathcal{S}_{\text{all}}^{\text{test}}$
2. Train with $\mathcal{S}_{\text{normal}}^{\text{train}}$ to maximize $\sum_i \log p(\mathbf{x}_i | \text{normal}) \forall \mathbf{x}_i \in \mathcal{S}_{\text{normal}}^{\text{train}}$
3. Infer using test case CXRs ($\mathbf{x}_i \in \mathcal{S}_{\text{all}}^{\text{test}}$) to obtain $\log p(\mathbf{x}_i | \text{normal})$.

The second metric is a logarithm probability (logarithm likelihood ratio hereafter), $\log p(\text{normal} | \mathbf{x}_i)$, which represents the probability that \mathbf{x}_i belongs

to the normal CXRs, which is equivalent to the probability derived in the discriminative model.

The function can be derived using Bayes’ theorem:

$$\log p(\text{normal}|\mathbf{x}_i) = \log p(\mathbf{x}_i|\text{normal}) + \log p(\text{normal}) - \log p(\mathbf{x}_i), \quad (2)$$

where $\log p(\text{normal})$ is a finite constant independence of the input CXRs (\mathbf{x}_i) and $\log p(\mathbf{x}_i)$ can be directly estimated by flow-based DNNs trained with $\mathcal{S}_{\text{all}}^{\text{train}}$. Note that the value of the constant does not affect receiver operation characteristic (ROC) curves, $\log p(\mathbf{x}_i)$ represents the likelihood that how accurately an input CXR (\mathbf{x}_i) is approximated with $\mathcal{S}_{\text{all}}^{\text{train}}$, and $\log p(\mathbf{x}_i|\text{normal})$ represents the likelihood that how accurately an input CXR (\mathbf{x}_i) is approximated with $\mathcal{S}_{\text{normal}}^{\text{train}}$. The above equation can be viewed as a simplified version of the equations introduced in [12].

The procedures to compute the second metric is summarized as follows:

1. Prepare input data:
 - (a) Gather CXR set, $\mathcal{S}_{\text{normal}}^{\text{train}}$
 - (b) Gather CXR set, $\mathcal{S}_{\text{all}}^{\text{train}}$ and $\mathcal{S}_{\text{all}}^{\text{test}}$
2. Train with $\mathcal{S}_{\text{normal}}^{\text{train}}$ to maximize $\sum_i \log p(\mathbf{x}_i|\text{normal}) \forall \mathbf{x}_i \in \mathcal{S}_{\text{normal}}^{\text{train}}$
3. Train with $\mathcal{S}_{\text{all}}^{\text{train}}$ to maximize $\sum_i \log p(\mathbf{x}_i) \forall \mathbf{x}_i \in \mathcal{S}_{\text{all}}^{\text{train}}$
4. Infer with the DNN trained in 2, using test CXRs ($\mathbf{x}_i \in \mathcal{S}_{\text{all}}^{\text{test}}$) to obtain $\log p(\mathbf{x}_i|\text{normal})$
5. Infer with the DNN trained in 3, using test CXRs ($\mathbf{x}_i \in \mathcal{S}_{\text{all}}^{\text{test}}$) to obtain $\log p(\mathbf{x}_i)$
6. Compute $\log p(\text{normal}|\mathbf{x}_i)$ for all the test CXRs using Eq. 2

3. Experiment

3.1. Experimental data

The CXRs used in this study were taken originally from the Radiological Society of North America Pneumonia Detection Challenge dataset and refined in [13]. This dataset comprises 30,000 frontal-view chest radiographs, with each image labeled as Normal, No Opacity/Not Normal, or Opacity by one to three board-certified radiologists. The Opacity group consists of images with suspicious opacities suggesting pneumonia, and the No Opacity/Not Normal group consists of images with abnormalities other than pneumonia.

Table 1: Composition of three sets. The number in brackets represents the number of overlapping normal CXRs in the two sets

Set	Num. normal CXRs	Num. abnormal CXRs
$\mathcal{S}_{\text{normal}}^{\text{train}}$	7,808 (6,529)	0
$\mathcal{S}_{\text{all}}^{\text{train}}$	6,553 (6,529)	6,631
$\mathcal{S}_{\text{all}}^{\text{test}}$	1,358	15,221

The composition of the CXR sets used in the present experiments is shown in Table 1. In the present study, the labels with the three categories are utilized only for inference (testing), and the distinction between ‘‘Opacity’’ and ‘‘No Opacity/Not Normal’’ is eliminated in the training.

3.2. Experimental setup

The original Glow code [11, 14] is utilized in the present study. The hyperparameters applied in this study are enumerated in Table 2.

Coupling layer	Affine
Flow permutation	1×1 convolution
Mini-batch size	128
Levels	7
Depth per level	32
Image size (in pixel)	512×512
Input vector dimension (N)	262,144
Total epochs	200

For the back-end of the DNNs, Tensorflow 1.12.0 is utilized with four GPUs (NVIDIA Tesla P100 SXM2), implemented in one computational node. The computational hardware utilized is C1102-GP8 (Reedbush-L) in the Information Technology Center, The University of Tokyo.

4. Results

ROC curves obtained using the logarithm likelihood metric ($\log p(\mathbf{x}_i | \text{normal})$) with different lesion targets are shown in Fig. 4. For each curve, the AUC

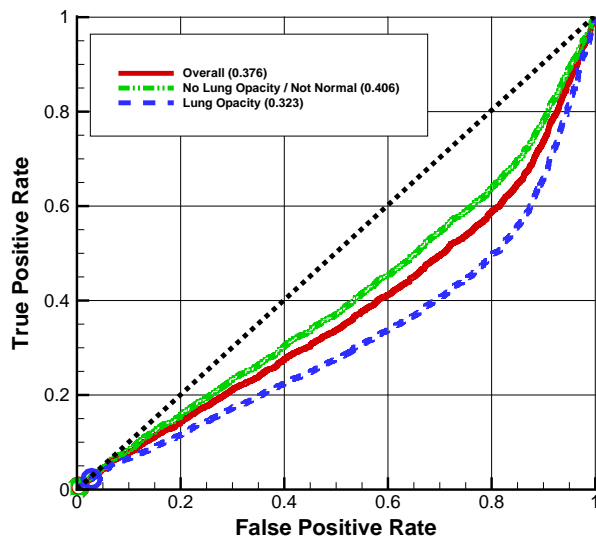


Figure 4: ROC curves obtained with the logarithm likelihood metric; AUCs are indicated in brackets for each label, and the circles represent cutoff points obtained from the Youden index.

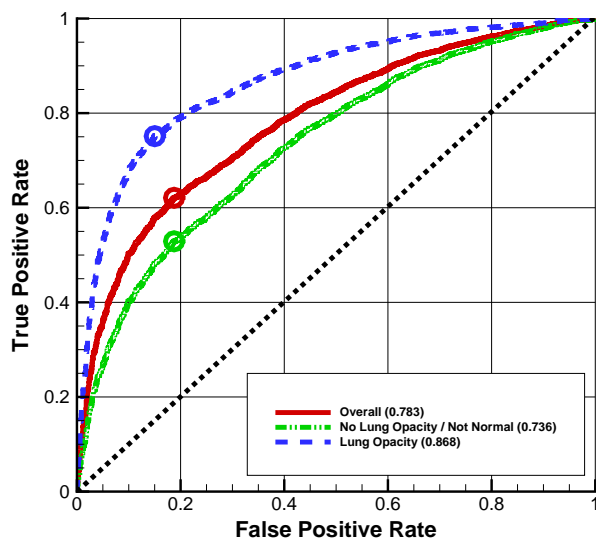


Figure 5: ROC curves obtained with the logarithm likelihood ratio metric; AUCs are indicated in brackets for each label, and the circles represent cutoff points obtained from the Youden index.

is much less than 0.5; hence, normal cases are likely to be judged as cases with high abnormality. These results have the same tendency as those in [12], where Fashion-MNIST was utilized as the in-distribution dataset (corresponding to normal CXRs in the present study) and MNIST was utilized as the out-of-distribution dataset (corresponding to abnormal CXRs in the present study).

ROC curves obtained using the logarithm likelihood ratio metric ($\sim \log p(\text{normal}|\mathbf{x}_i)$) with different lesion targets are shown in Fig. 5. Unlike the ROCs with the other metric, the overall AUC is approximately 0.783, indicating the efficacy of the logarithm likelihood ratio metric. Moreover, when limited to lung opacity cases, the corresponding AUC is approximately 0.868, which is comparable to results obtained with one of the most recent methods [6].

To clarify the reason for the inversion phenomenon for the logarithm likelihood metric, histograms of the two metrics and the relationships between the metrics and the proportion of zeros in a CXR were investigated. Figures 6(a) and 6(c) show normalized histograms with regard to the two metrics. Both the histograms have one peak for the normal label and two peaks for the anomaly labels. In the case of the metric based on the logarithm likelihood ratio, the peak for the normal label is shifted in the negative direction. However, in the case of the metric based on the logarithm likelihood, the peak for the normal label is shifted in the positive direction. This can directly affect the prediction accuracy of anomaly detection.

Figures 6(b) and 6(d) show the relationship between the negated metric value and the proportion of zeros in a CXR. There is a correlation between the proportion of zero pixels in a CXR and the likelihood; CXRs with many zero pixels tend to be judged as having higher normality. This means that background pixels over CXRs have high sensitivity if the logarithm likelihood metric is applied to detect anomalies, as pointed out in [12, 15]. However, there is no apparent correlation observed if the logarithm likelihood ratio metric is evaluated instead.

Figures 7–10 show the top 36 CXRs from all the test CXRs for different properties explained in the captions. With the logarithm likelihood metric (Figs. 7 and 8), a CXR of a child tends to be readily recognized as a CXR with higher normality, even if anomalies are included in the image, i.e., a false negative, whereas this issue does not arise for the other metric. The CXR of a child has many zero pixels, and is considered as the primary reason for the issue. There are no characteristic differences except for anomalies due

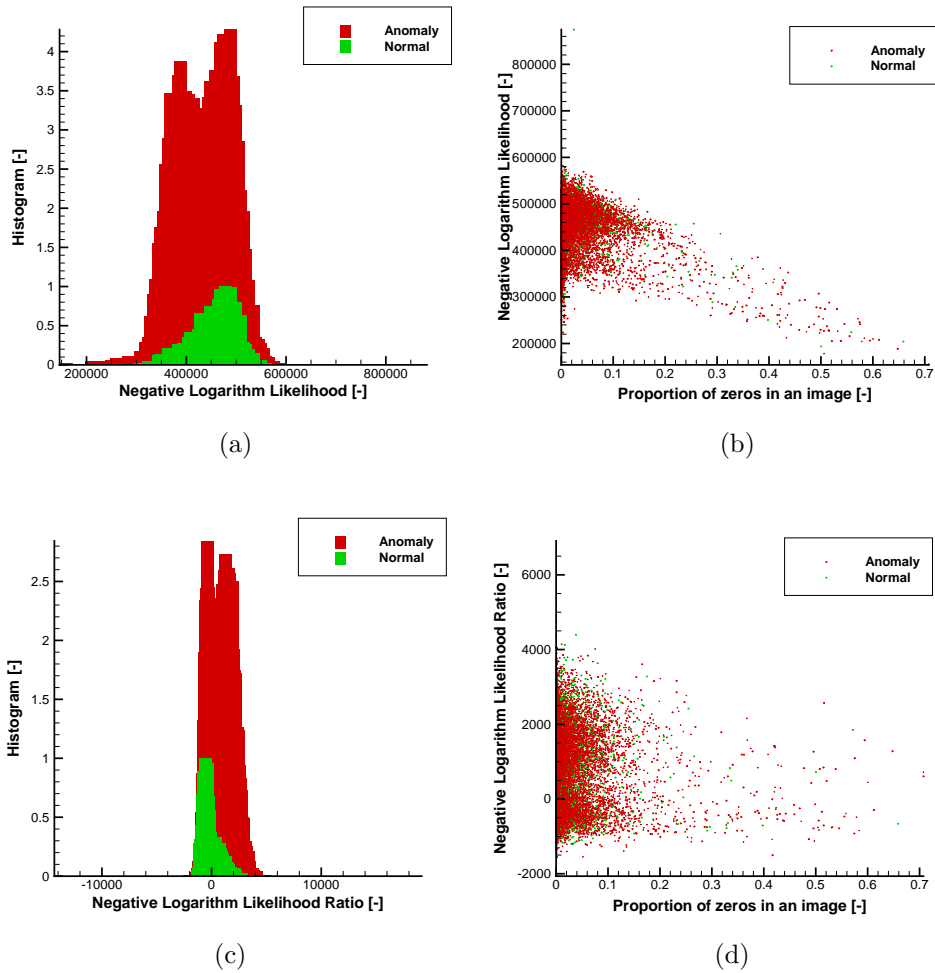


Figure 6: (a) Histogram of normal CXRs biased toward higher negative log-likelihoods. (b) Relationship between negative log-likelihoods and the proportion of zero pixels in a CXR. (c) Histogram of normal CXRs biased toward lower negative log-likelihood ratios. (d) Relationship between negative log-likelihood ratios and the proportion of zero pixels in a CXR.



Figure 7: Top 36 CXRs most likely to have an anomaly according to the logarithm likelihood metric.



Figure 8: Top 36 CXRs least likely to have an anomaly according to the logarithm likelihood metric.

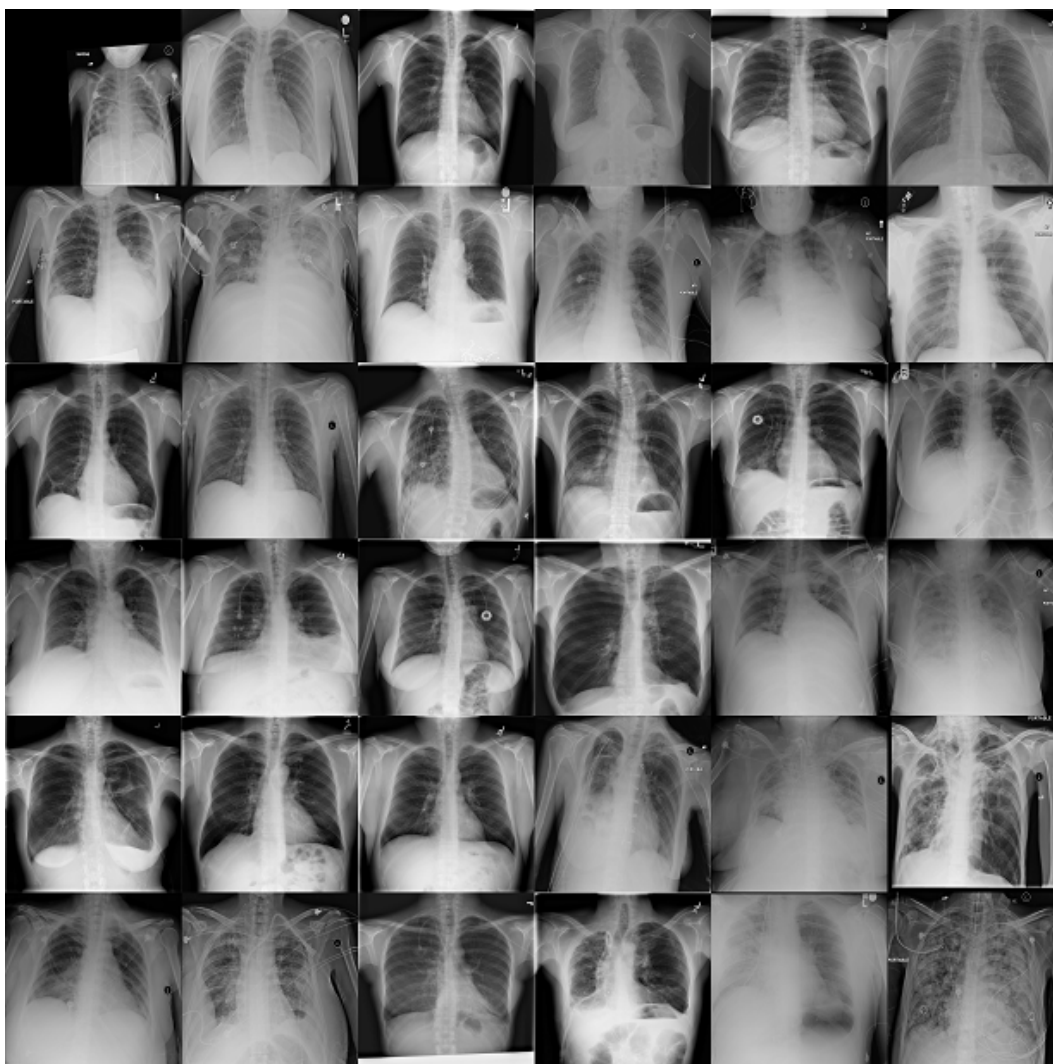


Figure 9: Top 36 CXRs most likely to have an anomaly according to the logarithm likelihood ratio metric.

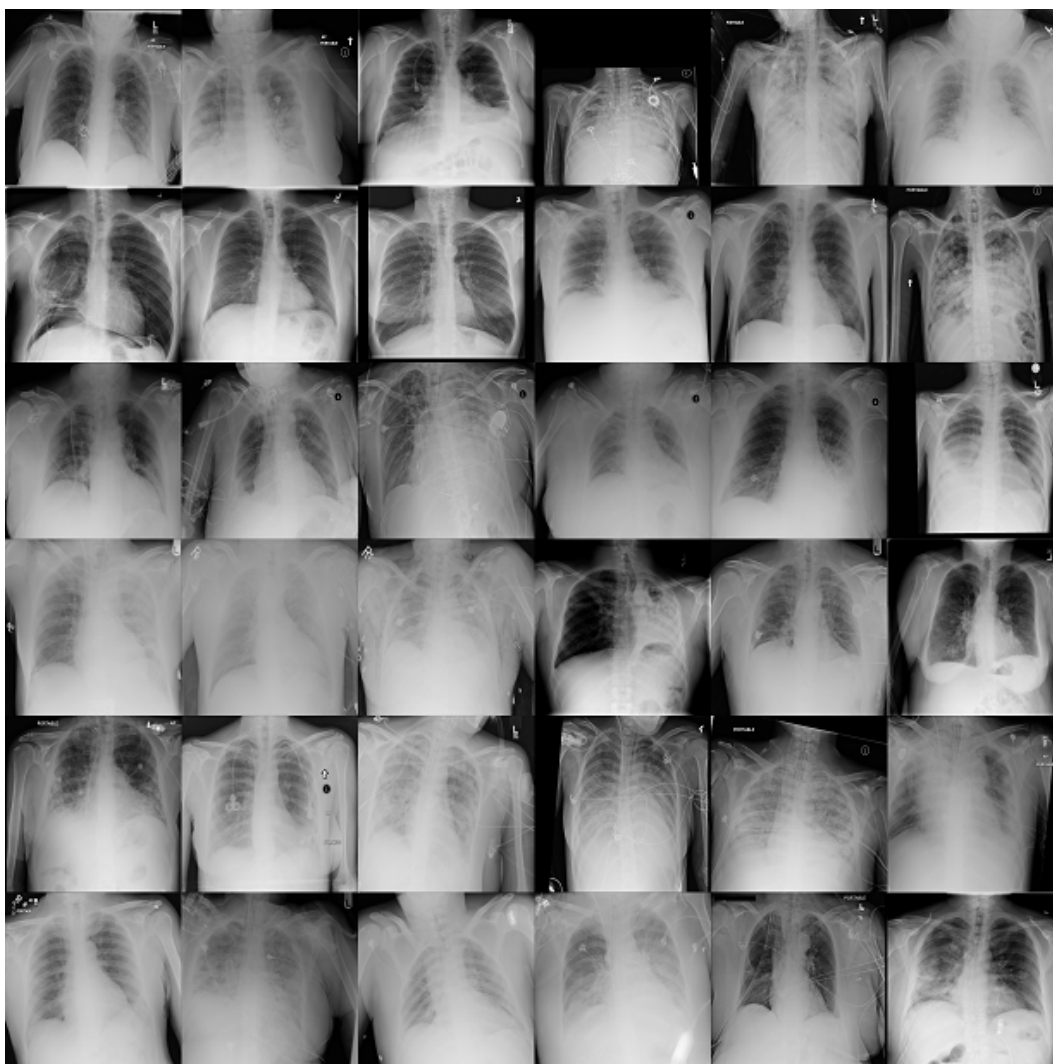


Figure 10: Top 36 CXRs least likely to have an anomaly according to the logarithm likelihood ratio metric.

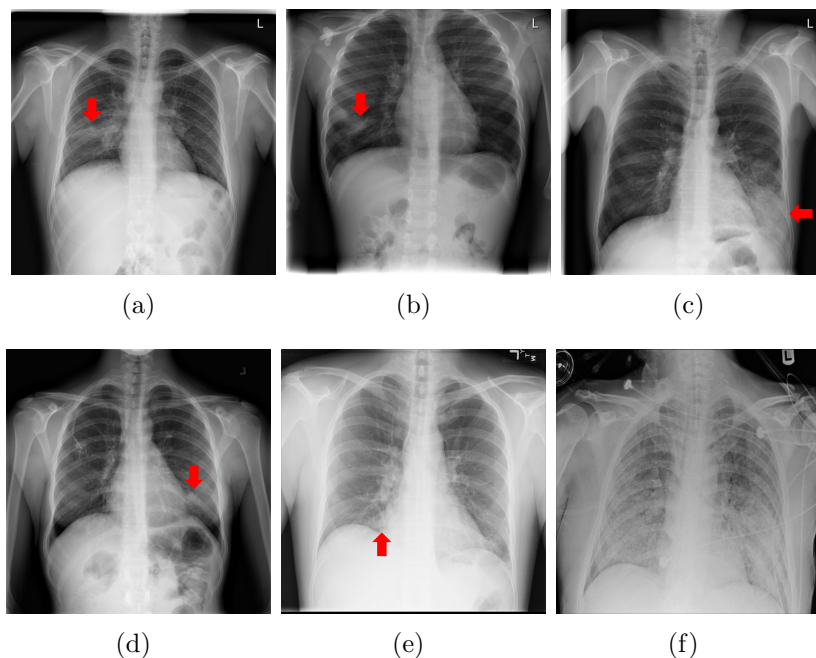


Figure 11: Typical CXRs with an abnormal opacity from among the top 1,000 CXRs most likely to have an anomaly according to the likelihood ratio metric out of the 15,221 CXRs with an anomaly; the lesion is indicated with a red arrow if applicable.

to lesions between Figs. 9 and 10.

Figure 11 shows typical CXRs with abnormal opacity from among the top 1,000 CXRs most likely to have an anomaly according to the likelihood ratio metric out of the 15,221 CXRs with an anomaly. Figure 12 shows typical CXRs with anomaly other than the abnormal opacity in top 1,000 CXRs more likely to be with anomaly according to the likelihood ratio metric over 15,221 CXRs with anomaly.

5. Discussion

There has been no previous research on DL methods for CXRs in which a flow-based generative model was applied to detect anomalies, to the best knowledge of the authors. As mentioned earlier, there are two fundamental models in DL methods: the discriminative model and the generative model. In addition, GANs utilize both models, and flow-based generative models belong to the latter. Flowcharts for anomaly detection methods with the

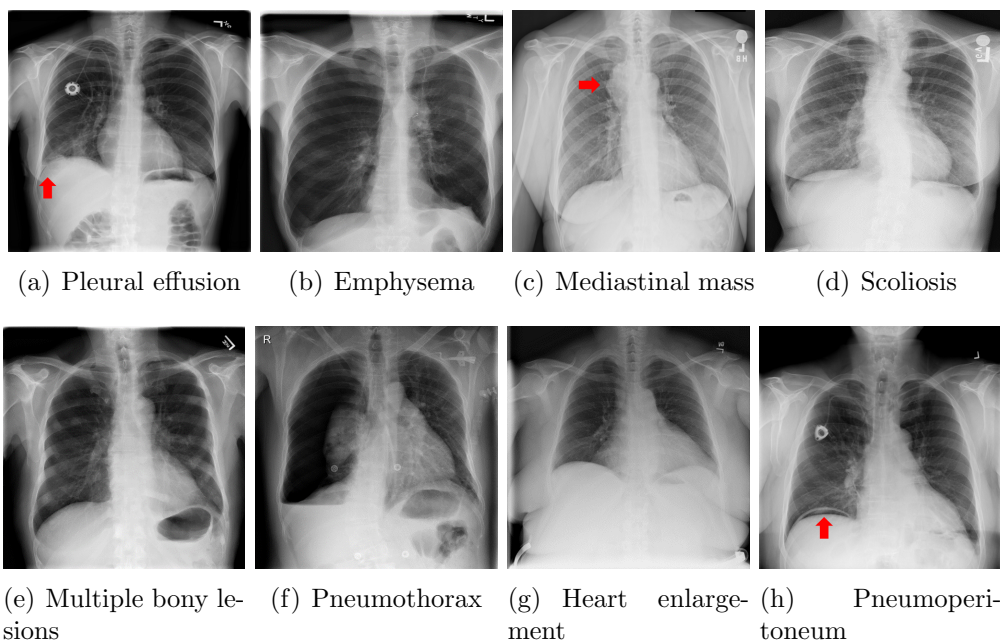


Figure 12: Typical CXRs with a lesion from among the top 1,000 CXRs most likely to have an anomaly according to the likelihood ratio metric out of the 15,221 CXRs with an anomaly excluding abnormal opacity; the lesion is indicated with a red arrow if applicable.

proposed model, the discriminative model, and GANs are shown in Fig. 2. Regarding the discriminative model, almost all the previous studies handled multiclassification problems, and only a few dealt with a binary classification problem. The models for both the multi- and binary classification problems (Fig. 2 (c)) are different from those in the present study (Figs. 2 (a, b)). Regarding the GAN (Fig. 2 (d)), Tang et al. [6] extended the model and solved one classification problem using a metric including the logarithm likelihood function $\log p(\text{normal}|\mathbf{x}_i)$, but additional terms and hyperparameters were also included in the metric.

With the present method, it is possible to evaluate the normality of inputted CXRs by preparing only two sets: a normal CXR set and a mixed set of normal and abnormal CXRs, such as all the CXRs in a clinic, both of which are relatively easy to acquire in clinical fields. Moreover, during the training procedure, only CXRs that are recognized as apparently normal can be selected to form the former set; with these characteristics, it is possible to reduce the workload of interpreters.

The fully supervised discriminative model attain a high AUC, e.g., $\text{AUC} \approx 0.99$ [4], in exchange for a high workload for labeling procedure for training. The weakly supervised discriminative model proposed by Tang et al. [7], in which both normal and abnormal CXRs are partially labeled, outputs a value of $\text{AUC} \approx 0.841$ with the NIH dataset [16]. Another weakly supervised discriminative model, in which only normal CXRs are labeled [6], has a lower $\text{AUC} (\approx 0.805)$ with the NIH dataset. Our results ($\text{AUC} \approx 0.783$ overall, $\text{AUC} \approx 0.868$ for lung opacity) are comparable to those given in [6].

If one of the most recent flow-based generative models, such as i-ResNet [17], is applied instead of Glow, higher computational costs are expected. On the other hand, with such a method, since the prediction accuracy of the logarithm likelihood is improved, a higher AUC is expected.

In this study we do not make assumptions about the images or even the input data dealt with; hence, the present method can be applied to other medical images, including surface data obtained by mammography and ultrasound imaging, and volume data obtained by computer tomography.

The present method only requires a set of normal CXRs in the labeling procedure; hence, the workload for the labeling can be greatly reduced. It is expected that the robustness and applicability of computer-aided diagnosis/detection (CAD) systems can be enhanced using this method. Finally, the present method can be considered as a key element in constructing CAD systems where volume medical data are handled; hence, the workload for the

labeling procedure is considerably higher than that for surface medical data.

The performance (AUC) of the present method is inferior to that of the most recent discriminative model with supervised learning. In addition, the proposed method cannot execute anomaly detection with multiple classification without modification. Future expected works are to extend the present study to 3-D CT medical image processing, and multiple classification of a dataset using a technique with which anomaly data are classified recursively as in [18].

6. Conclusions

We proposed a flow-based deep learning method combined with two metrics to detect anomalies in CXRs, where only the labeling of images belonging to a set of normal CXRs is required, and we tested the method using the Radiological Society of North America Pneumonia Detection Challenge dataset. The proposed method, in which the logarithm likelihood ratio metric is utilized, successfully detected anomalies in CXRs more precisely (overall AUC ≈ 0.783) than another method in which the logarithm likelihood metric is utilized (overall AUC ≈ 0.376). To summarize, the proposed method can be adopted to anomaly detection in CXRs with both acceptable precision and a low labeling workload.

Acknowledgements

The Department of Computational Diagnostic Radiology and Preventive Medicine, The University of Tokyo Hospital, is sponsored by HIMEDIC Inc. and Siemens Healthcare K.K. This work was supported in part by JSPS Grants-in-Aid for Scientific Research KAKENHI Grant Nos. 18K12095 and 18K12096. This work was also supported by the Joint Usage/Research Center for Interdisciplinary Large-scale Information Infrastructures and High Performance Computing Infrastructure projects in Japan (Project ID: jh190047-DAH).

References

- [1] G. Chassagnon, M. Vakalopoulou, N. Paragios, M.-P. Revel, Deep learning: definition and perspectives for thoracic imaging, *European Radiology* (2019). URL: <https://doi.org/10.1007/s00330-019-06564-3>. doi:10.1007/s00330-019-06564-3.

- [2] G. Litjens, T. Kooi, B. E. Bejnordi, A. A. A. Setio, F. Ciompi, M. Ghafoorian, J. A. Van Der Laak, B. Van Ginneken, C. I. Sánchez, A survey on deep learning in medical image analysis, *Medical Image Analysis* 42 (2017) 60–88.
- [3] B. Sahiner, A. Pezeshk, L. M. Hadjiiski, X. Wang, K. Drukker, K. H. Cha, R. M. Summers, M. L. Giger, Deep learning in medical imaging and radiation therapy, *Medical physics* 46 (2019) e1–e36.
- [4] P. Lakhani, B. Sundaram, Deep learning at chest radiography: Automated classification of pulmonary tuberculosis by using convolutional neural networks, *Radiology* 284 (2017) 574–582. doi:10.1148/radiol.2017162326.
- [5] D. S. Kermany, M. Goldbaum, W. Cai, C. C. S. Valentim, H. Liang, S. L. Baxter, A. McKeown, G. Yang, X. Wu, F. Yan, J. Dong, M. K. Prasadha, J. Pei, M. Y. L. Ting, J. Zhu, C. Li, S. Hewett, J. Dong, I. Ziyar, A. Shi, R. Zhang, L. Zheng, R. Hou, W. Shi, X. Fu, Y. Duan, V. A. N. Huu, C. Wen, E. D. Zhang, C. L. Zhang, O. Li, X. Wang, M. A. Singer, X. Sun, J. Xu, A. Tafreshi, M. A. Lewis, H. Xia, K. Zhang, Identifying medical diagnoses and treatable diseases by image-based deep learning, *Cell* 172 (2018) 1122–1131.e9. doi:10.1016/j.cell.2018.02.010.
- [6] Y. Tang, Y. Tang, M. Han, J. Xiao, R. M. Summers, Abnormal chest X-ray identification with generative adversarial one-class classifier (2019). URL: <https://ui.adsabs.harvard.edu/abs/2019arXiv190302040T>.
- [7] Y.-X. Tang, Y.-B. Tang, M. Han, J. Xiao, R. M. Summers, Deep adversarial one-class learning for normal and abnormal chest radiograph classification, volume 10950, SPIE, 2019. URL: <https://doi.org/10.1117/12.2511787>.
- [8] B. Park, Y. Cho, G. Lee, S. M. Lee, Y. H. Cho, E. S. Lee, K. H. Lee, J. B. Seo, N. Kim, A curriculum learning strategy to enhance the accuracy of classification of various lesions in chest-PA X-ray screening for pulmonary abnormalities, *Scientific Reports* 9 (2019) 15352. doi:10.1038/s41598-019-51832-3.

- [9] E. Çallı, K. Murphy, E. Sogancioglu, B. van Ginneken, FRODO: Free rejection of out-of-distribution samples: application to chest X-ray analysis (2019).
- [10] X. Yi, E. Walia, P. Babyn, Generative adversarial network in medical imaging: A review, *Medical Image Analysis* (2019) 101552.
- [11] D. P. Kingma, P. Dhariwal, Glow: Generative flow with invertible 1×1 convolutions, *Advances in Neural Information Processing Systems 2018-Decem* (2018) 10215–10224. [arXiv:1807.03039](https://arxiv.org/abs/1807.03039).
- [12] J. Ren, P. J. Liu, E. Fertig, J. Snoek, R. Poplin, M. A. DePristo, J. V. Dillon, B. Lakshminarayanan, Likelihood ratios for out-of-distribution detection (2019). URL: <http://arxiv.org/abs/1906.02845>. [arXiv:1906.02845](https://arxiv.org/abs/1906.02845).
- [13] G. Shih, C. C. Wu, S. S. Halabi, M. D. Kohli, L. M. Prevedello, T. S. Cook, A. Sharma, J. K. Amorosa, V. Arteaga, M. Galperin-Aizenberg, et al., Augmenting the National Institutes of Health chest radiograph dataset with expert annotations of possible pneumonia, *Radiology: Artificial Intelligence* 1 (2019) e180041.
- [14] Glow software, <https://github.com/openai/glow/>, 2019. [Online; accessed 19 November 2019].
- [15] J. Serrà, D. Álvarez, V. Gómez, O. Slizovskaia, J. F. Núñez, J. Luque, Input complexity and out-of-distribution detection with likelihood-based generative models, *arXiv preprint arXiv:1909.11480* (2019).
- [16] X. Wang, Y. Peng, L. Lu, Z. Lu, M. Bagheri, R. M. Summers, Chestx-ray8: Hospital-scale chest x-ray database and benchmarks on weakly-supervised classification and localization of common thorax diseases, in: *Proceedings of the IEEE Conference on Computer Vision and Pattern Recognition*, 2017, pp. 2097–2106.
- [17] J. Behrmann, W. Grathwohl, R. T. Q. Chen, D. Duvenaud, J.-H. Jacobsen, Invertible residual networks, in: K. Chaudhuri, R. Salakhutdinov (Eds.), *Proceedings of the 36th International Conference on Machine Learning*, volume 97 of *Proceedings of Machine Learning Research*, PMLR, Long Beach, California, USA, 2019, pp. 573–582. URL: <http://proceedings.mlr.press/v97/behrmann19a.html>.

- [18] H. H. Pham, T. T. Le, D. Q. Tran, D. T. Ngo, H. Q. Nguyen, Interpreting chest X-rays via CNNs that exploit disease dependencies and uncertainty labels, arXiv preprint arXiv:1911.06475 (2019).